

Department of Physics and Astronomy  
University of Heidelberg

Bachelor Thesis in Physics  
submitted by

**Lars Heinen**

born in Mönchengladbach (Germany)

**2017**



# Setup and Characterization of a Single-Focused Beam Optical Trap for Lithium

This Bachelor Thesis has been carried out by  
Lars Heinen  
at the Max-Planck-Institut für Kernphysik  
in Heidelberg  
under the supervision of  
Priv.-Doz. Dr. Alexander Dorn  
and  
Prof. Dr. Thomas Pfeifer



## **Zusammenfassung:**

Im Rahmen dieser Arbeit wurde eine neue optische Falle als Teil des größeren MOTREMI-Experiments am Max-Planck-Institut für Kernphysik aufgebaut. Die bereits installierte magneto-optische Falle ist in der Lage  ${}^6\text{Li}$  Atome bis auf etwa  $100\ \mu\text{K}$  herunterzukühlen. Aus den Atomen wird so ein ultrakaltes Lithiumgas erzeugt, das im Zentrum der Hauptvakuumkammer gespeichert wird. Im zukünftigen Verlauf des Experiments sollen noch kältere Temperaturen erreicht werden, um so Ionisationsexperimente an entarteten Quantengasen durchführen zu können. Mit Hilfe der hohen Leistung eines stark rotverschobenen fokussierten Laserstrahls, ist es möglich, Lithiumatome auf Temperaturen von  $100\ \text{nK}$  zu kühlen. Um eine erhöhte Fallenlebensdauer zu erreichen, wurde eine Intensitätsregelung konstruiert. Durch die Verwendung von zwei unterschiedlichen Photodioden wird jeder Leistungsbereich des Lasers abgedeckt. Die hohen Leistungen, die in der Falle verwendet werden, verursachen thermische Effekte im Aufbau. Dadurch können sich die spezifischen Eigenschaften der verwendeten optischen Elemente als auch die des Lasers selbst ändern. Im Zuge dessen wurden die thermischen Effekte quantitativ untersucht. Neben der Verschiebung und Verkleinerung des fokussierten Strahls für konvexe Linsen, wurde auch der Effekt auf die Fallengröße des Lasers festgestellt.

## **Abstract:**

Within the MOTREMI experiment at the Max-Planck-Institut für Kernphysik a new optical trap was constructed. A already installed magneto-optical trap cools  ${}^6\text{Li}$  atoms down to temperatures on the order of  $100\ \mu\text{K}$ . From the corresponding atoms an ultracold lithium gas is trapped inside the center of the main vacuum chamber. In the further course of the experiment, ionization measurements with a degenerate quantum gas will be carried out. In order to create these gases, one needs to surpass the temperature limit of the magneto-optical trap. Traps using a high intensity, far red-detuned focused laser beam are able to achieve temperatures on the order of  $100\ \text{nK}$ . An intensity stabilization which is able to extend the lifetime of trapped gas was constructed in the scope of this thesis. With the use of two different photodiodes, every intensity level of the laser is covered. The high laser powers which are needed for the trap, can lead to thermal effects in the entire setup. Consequently, the properties of the laser and the optical elements the laser is passing through can change. Therefore, a quantitative analysis of these thermal effects has been carried out. Besides the shift and reduction of the focused laser beam, the thermal effect on the trap size was obtained.



# Contents

<b>1</b>	<b>Introduction and Motivation</b>	<b>1</b>
<b>2</b>	<b>Laser Cooling</b>	<b>3</b>
2.1	The Spontaneous Force . . . . .	3
2.2	Doppler Cooling . . . . .	5
2.3	Magneto-Optical Trap . . . . .	7
2.4	Red-detuned Optical Dipole Trap . . . . .	9
2.5	Evaporative Cooling . . . . .	10
<b>3</b>	<b>Implementation of an Optical Dipole Trap</b>	<b>13</b>
3.1	Setup of the Optical Dipole Trap . . . . .	13
3.2	Setup of the Intensity Stabilization . . . . .	14
3.3	Transferring Atoms into the Optical Dipole Trap . . . . .	15
<b>4</b>	<b>Consequences of High Intensity Lasers</b>	<b>19</b>
4.1	Theory of Thermal Lensing . . . . .	19
4.1.1	The Gaussian Beam . . . . .	19
4.1.2	The Thermal Lens . . . . .	21
4.2	Quantitative Observation of Thermal Effects . . . . .	22
4.2.1	Beam Quality . . . . .	23
4.2.2	Focus Shift . . . . .	26
4.2.3	Divergence Change . . . . .	29
<b>5</b>	<b>Conclusion and Outlook</b>	<b>35</b>



# 1 Introduction and Motivation

Often, theoretical discoveries in physics take years until they are tested by experiments. Required techniques and technology have to be developed before the basis of quantitative analysis can be formed. In the case of Bose-Einstein condensates (BECs), it took over 70 years until the technology was advanced enough and a first condensate was created [AEM<sup>+</sup>95].

The problem is that the transition of a gas to a BEC requires noninteracting bosonic atoms at temperatures so low, that the thermal de Broglie wavelength  $\lambda_{dB}$  becomes larger than the mean spacing between atoms. For densities of  $n = 7 \cdot 10^{13} \text{ cm}^{-3}$  the critical temperature at which quantum statistics become important is  $T = 1 \mu\text{K}$ . For real gases the interaction between atoms within the gas is very important, since it alters the properties of the transition to the BEC. The scattering length  $a$  quantizes the interaction between ultracold atoms [Let07].

In the experiment described in this thesis, the fermionic atom  ${}^6\text{Li}$  will be condensed into a BEC by using the property of so-called Feshbach resonances. By setting up an external magnetic field, the scattering length is influenced. Altering the magnetic field, the scattering length can be tuned such that the interaction between the atoms form a bosonic  $\text{Li}_2$  molecule.

The later analysis of the condensate will be performed in a *Reaction Microscope* (REMI). In the first stage single  ${}^6\text{Li}$  atoms, and in the second stage weakly bound  $\text{Li}_2$  molecules are ionized by a femtosecond laser pulse. The recoil electrons and ions are guided by electric and magnetic fields to detectors on both sides of the vacuum chamber. With the precise determination of the impact, it is possible to reconstruct transversal and longitudinal momenta.

However, the lithium atoms have to be cooled in the first place. Since degenerate gases require temperatures on the order of a few hundred nK, atoms from an oven vapor have to be cooled by several orders of magnitude. A common starting point for a quantum degenerate gas is the operation of a magneto-optical trap. With this apparatus, it is possible to trap and cool down atoms to temperatures of a few hundred  $\mu\text{K}$  and create phase space densities on the order of  $10^{-4}$ . Further cooling is done by the use of an optical dipole trap which forms a conservative trapping potential. Far red-detuned high intensity lasers are normally used in order to surpass the temperature limits of magneto-optical traps.

## *1 Introduction and Motivation*

Within the scope of this bachelor thesis a setup of a single-focused beam trap was realized. From the already existing magneto-optical trap, the atoms will be transferred into the new one. By performing evaporative cooling, the trap will cool  ${}^6\text{Li}$  atoms down to sufficient temperatures from where the creation of a quantum degenerate gas is possible. In order to maximize transfer and cooling efficiency, an intensity stabilization of the dipole laser was constructed. Because the laser has a very high intensity, thermal effects in the setup occur. Therefore, a quantitative analysis of varying trap properties, due to thermal heating, was carried out.

## 2 Laser Cooling

This chapter provides an introduction to the theory of cooling techniques with lasers. After providing information on the interaction between atoms and light, the reader gets to know how trapping and cooling of atoms is realized in this experiment.

### 2.1 The Spontaneous Force

As a starting point for the theoretical treatment of laser cooling, the interaction between near-resonant, monochromatic light and atoms is the electric dipole approximation, i.e. coupling of a classical electromagnetic field to the electric dipole of atoms is considered.

Cooling atoms with laser relies on effective directional transfer of momentum from photons of the light field to atoms it is interacting with. The effective directional momentum transfer is composed of repeated cycles of stimulated absorption and spontaneous emission. Each absorbed photon transfers momentum of

$$\Delta \vec{p} = \hbar \vec{k} , \quad (2.1)$$

where  $\vec{k}$  refers to the wave-vector of the photon. Due to the energy transfer induced by  $E = h\nu$  ( $\nu$  is the frequency of the photon) one outer shell electron moves into a higher quantum state. After the spontaneous decay of this excited state into a lower state one photon of the energy difference will be re-emitted. Emission of these photons on average occurs isotropically. Therefore, the mean value over many photon emissions leads to a momentum change of zero.

A clear distinction has to be made from the stimulated emission, which has a well-defined direction, because of interaction with the light field: the emitted photon always follows the direction of light. Since absorbed and re-emitted photon always has the same momentum direction, it does not induce an effective momentum change. Thus, it is neglectable in laser cooling.

Averaging over many cycles the net momentum change is in direction of the laser field and only contributes to the recoil of stimulated absorption. Therefore, the momentum difference per time is described by the spontaneous force

## 2 Laser Cooling

$$\vec{F}_{sp} = \hbar \vec{k} \gamma_{scat} . \quad (2.2)$$

$\gamma_{scat}$  denotes the scattering rate of photons per time interval. This scattering rate depends on the lifetime-dependent *damping factor*  $\gamma = \frac{1}{\tau}$  of the energy transition, where  $\tau$  is the lifetime of the excited state, the laser intensity  $I$ , the *saturation intensity*  $I_s$ , which is specific for each energy transition of an atom, and the *laser detuning* from the atomic resonance  $\delta_0 = \omega_l - \omega_0$ , where  $\omega_l$  is the laser frequency and  $\omega_0$  is the atomic resonance frequency. The scattering rate is given by

$$\gamma_{scat} = \frac{\gamma}{2} \frac{s_0}{1 + s_0 + (2\delta_0/\gamma)^2} , \quad (2.3)$$

where  $s_0 = I/I_s$  is the saturation parameter [Mes07].  $I_s$  is defined as the necessary intensity to excite 1/4 of the atoms at a detuning of  $\delta_0 = 0$ . Using equation (2.3) the spontaneous force is

$$\vec{F}_{sp} = \frac{\hbar \vec{k}}{2} \frac{\gamma s_0}{1 + s_0 + (2\delta_0/\gamma)^2} . \quad (2.4)$$

In the limit  $s_0 \rightarrow \infty$  the scattering rate approaches the value of  $\gamma/2$ . Thus, the maximum spontaneous force is

$$\vec{F}_{sp}^{max} = \hbar \vec{k} \frac{\gamma}{2} . \quad (2.5)$$

In figure 2.1 the scattering rate is plotted over detuning for different saturation parameters. By using laser intensities  $I \gg I_0$  one can clearly see that the scattering rate reaches a higher maximum at  $\delta_0 = 0$ . Also for  $\delta_0 \neq 0$  the drop off is not as sharp as for lower  $s_0$ . This effect is known as *power broadening*.

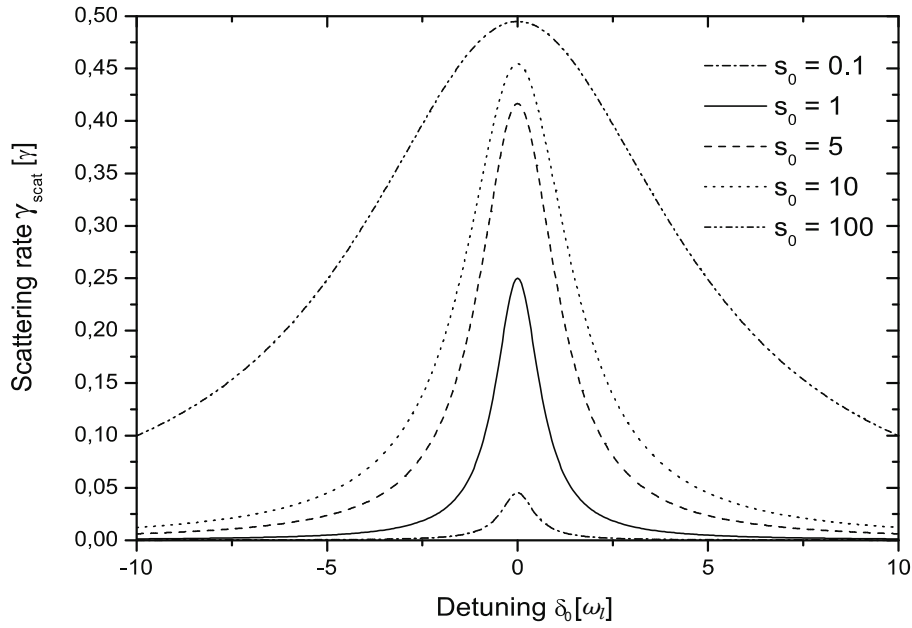


Figure 2.1: Scattering rate  $\gamma_{scat}$  over detuning for different values of saturation parameter  $s_0$  [Ste07]

## 2.2 Doppler Cooling

Taking into account that the atoms are not at rest, one has to consider the Doppler effect. In the reference frame of an atom with velocity  $\vec{v}$  the laser frequency  $\omega_l$  is red- or blue-shifted depending on the motion of the atom. Including the frequency shift, the detuning is

$$\delta_{dopp} = \omega_l - \omega_0 - \vec{k} \cdot \vec{v}. \quad (2.6)$$

Blue Doppler shifts are produced by counterpropagating atoms and photons. In order to have a spontaneous force dependent on the Doppler shift, one can simply plug equation (2.6) into (2.4)

$$\vec{F}_{sp}(\vec{v}) = \frac{\hbar \vec{k}}{2} \frac{\gamma s_0}{1 + s_0 + (2\delta_{dopp}/\gamma)^2} \quad (2.7)$$

By detuning the beams red with respect to atomic transition frequency ( $\delta_0 = \omega_l - \omega_0 < 0$ ), atoms see the beam counterpropagating closer to resonance, because of the positive Doppler shift. One-dimensional *optical molasses* (OM) use two counterpropagating overlapping laser beams. Using intensities where stimulated emission is neglectable, the forces add up to

## 2 Laser Cooling

$$\vec{F}_{OM} = \vec{F}_+ + \vec{F}_-, \quad (2.8)$$

using equation (2.7)

$$\vec{F}_\pm(\vec{v}) = \pm \frac{\hbar \vec{k}}{2} \frac{\gamma s_0}{1 + s_0 + (2\delta_\pm/\gamma)^2}$$

with

$$\delta_\pm = \delta_0 \mp \vec{k} \cdot \vec{v}.$$

Neglecting terms of order  $(kv/\gamma)^2$  and higher, the sum leads to a linearization in  $v$ , resulting in a viscous damping term in the equation of motion of the atom [Ste07]

$$F_{OM} \cong \frac{8\hbar k^2 \delta s_0}{\gamma[1 + s_0 + (2\delta/\gamma)^2]^2} v \equiv -\alpha v \propto -v. \quad (2.9)$$

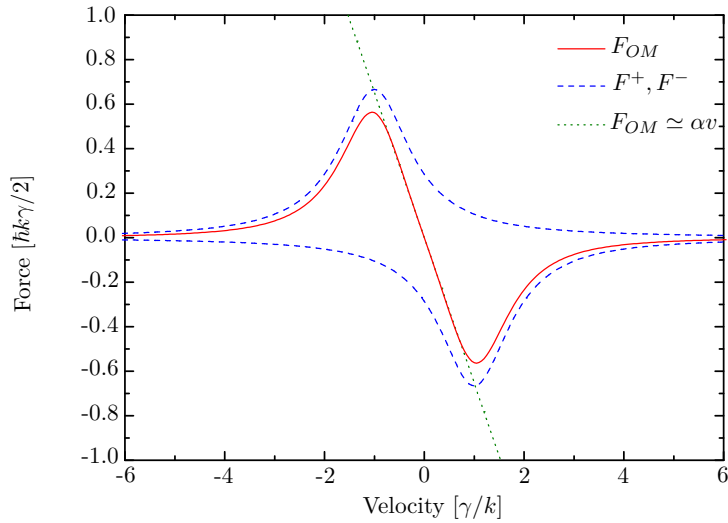


Figure 2.2: Velocity-dependent force  $F$  in units of  $F_{max}$  in an one-dimensional optical molasses. The blue dashed line shows the beam forces  $F^+$  and  $F^-$  respectively for each direction of the laser beam and  $F_{OM}$  is indicated by the red line. All forces are calculated for  $\delta_0 = \gamma$  and  $s_0 = 2$ . For small velocities the linear approximation of the force is shown by the green dotted line [MS99].

## 2.3 Magneto-Optical Trap

In order to create a three-dimensional OM, six laser beams are needed, while two beams counterpropagate for each dimension. The overlap of these beams provides a velocity-dependent damping force in three dimensions. To keep atoms localized in this overlap, it is necessary to also have a position-dependent force. By applying an anti-Helmholtz configuration, a magnetic quadrupole is created. This magnetic quadrupole has to be set such that in the intersect of the laser beams the magnetic field is zero.

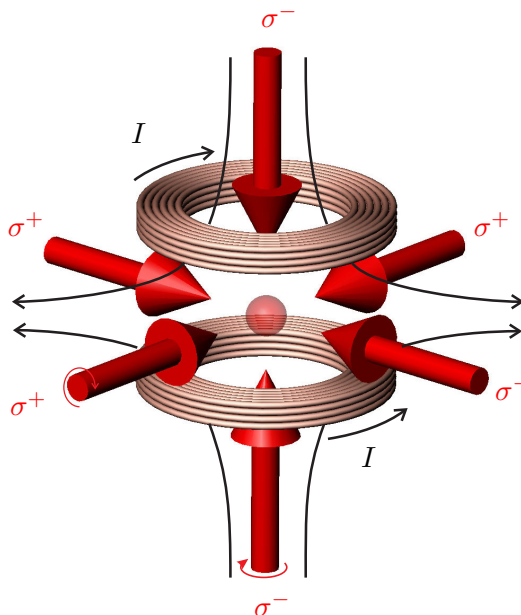


Figure 2.3: Principle of a three-dimensional MOT. The coils create a spherical magnetic quadrupole. Three circularly polarized laser beams provide the trapping force [Ste07].

To explain how such an arrangement forms a so-called *magneto-optical trap* (MOT), it is useful to simplify to the one-dimensional case. Assume the atom only has a ground state  $|g\rangle$  of total angular momentum  $F = 0$  and an excited state  $|e\rangle$  of total angular momentum  $F = 1$ . In this simplified picture atomic transitions with the scheme of  $F_g = 0 \rightarrow F_e = 1$  have three Zeeman components in a magnetic field. Each of these is excited by a different polarization  $\pi, \sigma^\pm$ . In figure 2.4 a simplified energy level diagram of an one-dimensional MOT is demonstrated. In the centre of the trap ( $z=0$ ) the lasers are out of resonance, because they are red-detuned as mentioned in the previous section. If an atom is moving out of the trap, the

## 2 Laser Cooling

Zeeman components tune with the magnetic field. Therefore the magnetic field provides a position-dependent shift. For  $B > 0$  the magnetic field shifts the energy level of  $m_{F_e} = -1$  closer to resonance, while  $m_{F_e} = +1$  is tuned out of resonance. If  $\sigma^-$ -polarized light is interacting from the right, more photons are scattered from the  $\sigma^-$ -polarized beam than from the  $\sigma^+$ -polarized one. The effect is analogous for atom motion in the other direction, where  $B < 0$  and the energy shift of  $m_{F_e} = +1$  is tuned into resonance. This leads to a net spatial-dependent force towards the trap center, similar to the velocity-dependent force in optical molasses. Any system with  $F_g \rightarrow F_e = F_g + 1$  is described well under these simplified assumptions.

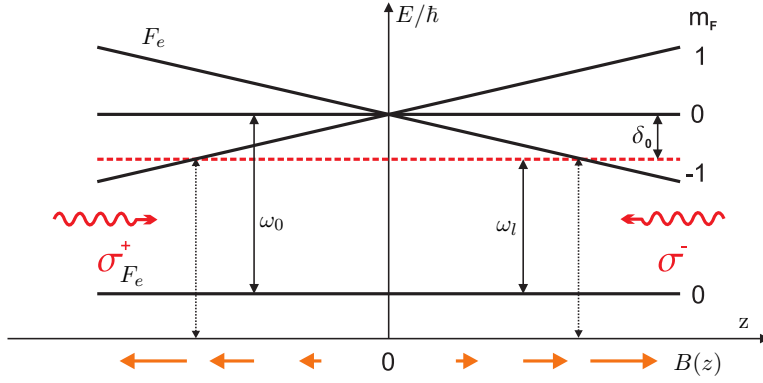


Figure 2.4: Principle of an one-dimensional MOT

By introducing this magnetic quadrupole, the detuning from (2.8) gets modified to

$$\delta_{\pm}(z) = \delta_0 \mp \vec{k} \cdot \vec{v} \pm \frac{\Delta\mu B(z)}{\hbar} \quad (2.10)$$

where  $\Delta\mu = \mu_e - \mu_g$  with  $\mu_e, \mu_g$  corresponding to the involved magnetic momenta of the excited and ground state.

Plugging  $\delta_{\pm}(z)$  into equation (2.8) and assuming  $|kv| \ll \gamma$  and  $|(\Delta\mu B_z/\hbar)z| \ll \gamma$ , one obtains

$$\begin{aligned} F_{MOT} &\cong \hbar k^2 \frac{8\delta s_0}{\gamma[1+s_0+(2\delta/\gamma)^2]^2} v + \hbar k \frac{\Delta\mu B_z}{\hbar} \frac{8\delta s_0}{\gamma[1+s_0+(2\delta/\gamma)^2]^2} z \\ &\equiv -\beta v + \kappa z, \end{aligned} \quad (2.11)$$

which describes a damped harmonic oscillator. Thus, atoms perform a damped harmonic oscillation with a potential minimum in the trap center.

Equation (2.11) leads to a damping rate of  $\beta = \alpha/(2m)$  and oscillation frequency of  $\omega = \sqrt{\kappa/m}$ .

### Temperature of Magneto-Optical Traps

Since atoms are cooled by effective momentum transfer via scattering with a resonant photon averaged over many cycles of stimulated absorption followed by spontaneous emission, it leads to a diffusive spreading of the mean squared momentum resulting in a heating rate

$$\dot{E}_{heat} = \frac{1}{2m} \frac{d}{dt} \langle p^2 \rangle. \quad (2.12)$$

This results in a lower limit for the temperature achievable by a solely scattering based cooling technique, called *Doppler limit* or *Doppler temperature* given by

$$T_D(\delta) = \frac{\hbar\gamma}{4k_B} \frac{1 + (2\delta_0/\gamma)^2}{(|\delta_0|/\gamma)}. \quad (2.13)$$

Within the one-dimensional model of a MOT, the Doppler temperature is minimal at a detuning of  $\delta = -\gamma/2$

$$T_{D_{min}} = \frac{\hbar\gamma}{2k_B}. \quad (2.14)$$

In order to create quantum degenerate gases, temperatures below the Doppler limit have to be reached. One solution to this problem is to transfer them into a trap, which does not rely on Doppler cooling. In the next section basic principles of an optical dipole trap, which creates a conservative trapping potential from induced electric dipoles in atoms, will be explained.

## 2.4 Red-detuned Optical Dipole Trap

Ultracold gases with temperatures  $\sim 1\text{mK}$  can easily be achieved with Doppler cooling. However, the creation of Bose-Einstein condensates requires temperatures on the order of  $\sim 10^{-7}\text{K}$ . To get atoms in such a low energy state, further cooling is necessary which can be carried out by the following technique.

Atoms are no longer trapped by a spatial and velocity depended trap, but a conservative potential. It is created via the averaged interaction energy of the electric field with the induced electric dipole of the atoms.

Hereinafter the basic concepts of trapped atoms in optical dipole potentials are introduced by using a simplified approach of a classical model:

Placing an atom into laser light with an electric field of

$$\vec{E}(\vec{r}, t) = \vec{e} \tilde{E}(\vec{r}) e^{-i\omega t} + c.c. \quad (2.15)$$

## 2 Laser Cooling

the resulting atomic dipole moment is

$$\vec{p}(\vec{r}, t) = \vec{e} \tilde{p}(\vec{r}) e^{-i\omega t} + c.c. , \quad (2.16)$$

which oscillates at driving frequency  $\omega$ . The unit polarization vector is denoted by  $\vec{e}$ . The deriving dipole potential in the electric field is denoted by

$$U_{dip} = -\frac{1}{2} \langle \vec{p} \vec{E} \rangle , \quad (2.17)$$

where the brackets indicate a time average. For red-detuned traps the relative sign of  $\vec{E}$  and  $\vec{p}$  is positive. Thus,  $U_{dip}$  is a negative and therefore attractive potential. The depth of the trapping dipole potential

$$U_{dip}(\vec{r}) = -\frac{3\pi c^2}{2\omega_0^3} \left( \frac{\Gamma}{\omega_0 - \omega} + \frac{\Gamma}{\omega_0 + \omega} \right) I(\vec{r}) \quad (2.18)$$

depends on the natural linewidth  $\Gamma$  of the transition, the laser intensity  $I(\vec{r})$  and detuning  $(\omega_0 - \omega)$  of the laser light from the resonance frequency  $\omega_0$ . Since the scattering rate

$$\Gamma_{sc}(\vec{r}) = -\frac{3\pi c^2}{2\hbar\omega_0^3} \left( \frac{\omega}{\omega_0} \right)^3 \left( \frac{\Gamma}{\omega_0 - \omega} + \frac{\Gamma}{\omega_0 + \omega} \right)^2 I(\vec{r}) \quad (2.19)$$

drops off quadratically with growing detuning of the laser light and trap depth scales linearly, scattering can be suppressed at the cost of high intensities. A more detailed view on this topic can be found in [GWO00].

In order to achieve even lower temperatures, a cooling technique is applied which relies on losing atoms in the high-energy tail of the Maxwell-Boltzmann distribution, which is explained in the following section.

## 2.5 Evaporative Cooling

The principle of evaporative cooling will be derived by consideration of a gas, which is described by the *Maxwell-Boltzmann distribution*

$$f(v) = \sqrt{\left( \frac{m}{2\pi k_B T} \right)^3} 4\pi v^2 e^{-\frac{mv^2}{2k_B T}} \quad (2.20)$$

with  $v$  denoting velocity of a gas atom.  $T$  is the gas temperature,  $k_B$  the *Boltzmann constant* and  $m$  the mass of involved atoms. A main assumption is that atoms of the gas only interact via elastic scattering. This restriction is valid in first order until quantum effects need to be considered. The

probability density over speed of the particles is shown in figure 2.5. The distribution peaks in a maximum at

$$v_p = \sqrt{\frac{2kT}{m}} , \quad (2.21)$$

while the mean velocity is determined by

$$\langle v \rangle = \frac{2}{\sqrt{\pi}} v_p . \quad (2.22)$$

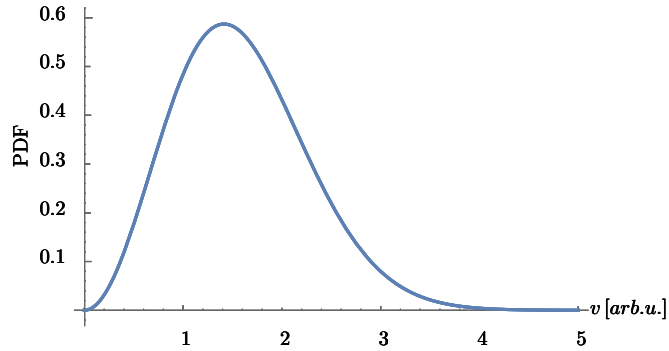


Figure 2.5: Maxwell-Boltzmann distribution of an arbitrary gas. Note that the graph shows the probability distribution function (PDF).

As can be seen in the distribution atoms are likely to have higher velocities than the average. Now consider the case of an attractive trap potential, which is able to hold atoms with velocity  $v \leq v_{trap}$  (the maximum velocity that the trap can hold is denoted by  $v_{trap}$ ). At this point here is a quick reminder that velocity corresponds directly to energy and temperature for a single particle as

$$\langle E_{kin} \rangle = \frac{1}{2} m \langle v^2 \rangle = \frac{3}{2} k_B T , \quad (2.23)$$

where the brackets denote the average. After some time almost all atoms which have greater velocity than  $v_{trap}$  will escape the trap. Thus, the amount of captured atoms decreases. After a certain time atoms rethermalize by elastic collisions. The new set can again be defined by a Maxwell-Boltzmann distribution, which describes a set of particles with lower mean velocity. This process goes on until a thermal equilibrium is reached. In this state only colder atoms are left. Thus, the average temperature is lower than before. This effect is called plain evaporative cooling.

## 2 Laser Cooling

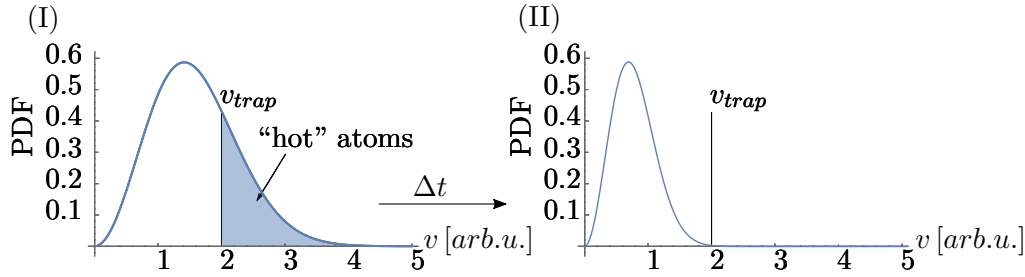


Figure 2.6: Change of velocity in trapped gas described by Maxwell-Boltzmann distribution. Setting the trap depth “cuts” the distribution at  $v = v_{trap}$  (I). After rethermalization time  $\Delta t_{th}$  the left atoms can be described by a new Maxwell-Boltzmann distribution (II).

In difference, forced evaporative cooling is done by lowering the trap potential depth (figure 2.7). Due to the change, again atoms with  $v > v_{trap}$  escape the trap. Besides the decrease of total atom number in the trap, also the mean temperature of the set decreases. Going on with this cycle, temperatures and densities can be achieved that are cold enough to open the door to quantum degenerate atomic samples.

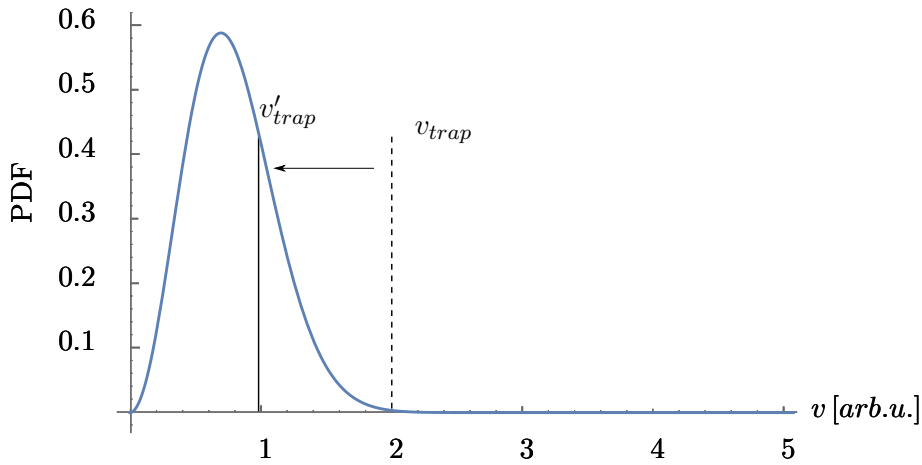


Figure 2.7: Maxwell-Boltzmann distribution with lowered trap velocity. From here on, the same procedure as shown in figure 2.6 starts.

In the case of optical dipole traps, the potential depth can be lowered by reducing the laser intensity. Performing forced evaporative cooling in the optical dipole trap, will be explained in the following chapter.

# 3 Implementation of an Optical Dipole Trap

As described in section 2.4, optical dipole traps are used to cool the lithium gas from MOT temperatures around 1 mK to temperatures of  $1 \mu\text{K}$  and below. This chapter reviews the steps taken to accomplish an optical dipole trap. The first section provides an overview of the setup that creates the trap. In the succeeding section, considerations towards losses from the trap, induced by fluctuations in the laser intensity, are carried out by the installation of a feedback system. Finally, the transfer of atoms from the MOT to the optical dipole trap is discussed.

## 3.1 Setup of the Optical Dipole Trap

There are several possible arrangements setting up an optical dipole trap. As part of this thesis a single focused-beam trap configuration was assembled. The extension to crossed beam traps is relatively easy to realize from the single focused-beam configuration. Similar to an one-dimensional MOT beam, the dipole laser can be retro-reflected by a set of mirrors on the opposite side of the vacuum chamber such that an overlap under a different angle is accomplished. However, single focused-beam traps are sufficient to trap atoms [GWO00].

Horizontal focused-beam traps are created by a focused Gaussian laser beam (see section 4.1.1 for details). Focusing the beam creates a three-dimensional anisotropic confinement. While the confinement in radial direction is symmetric and characterized by the beam diameter  $w_0$ , the trap dimension in axial direction is characterized by  $z_R = \pi w_0^2 / \lambda$ . Thus, the potential in radial direction is much steeper than in the axial direction. This property is important to accomplish stable traps. Because of the horizontal arrangement, it is possible to minimize perturbation caused by the gravitational force.

Figure 3.1 provides an overview of the setup installed within this project. The far red-detuned light comes from a 200W Ytterbium fiber laser (YLR-200-LP, IPG Photonics) which is power-tunable in a range of  $\sim 0.5 \text{ W}$  to  $\sim 200 \text{ W}$ . The fiber is maintaining single transversal mode and polarization. Therefore, it provides an almost perfect Gaussian beam with linear polarization. The wavelength of the laser is 1070 nm which is far red-detuned from the resonant 671 nm transition.

### 3 Implementation of an Optical Dipole Trap

Using a telescope with two lenses, which have focal lengths of  $f_1 = 100$  mm and  $f_2 = -50$  mm, the initial output beam diameter shrinks from 5 mm to 2.5 mm, since the active aperture of the used *acousto-optic modulator* (AOM)<sup>1</sup> is 3 mm. Later on, the AOM will be used to control forced evaporative cooling by modulating the beam power in the first order. Because of inefficiencies the maximum output into the diffracted first order is limited to 80% of the initial power. The diffraction angle between zeroth and first order is  $\alpha = 7$  mrad. Thus, the two orders need to be separated by an extended optical path length. A length of  $\sim 790$  mm is sufficient for satisfactory spacing of the orders. The zeroth order is guided into a beam dump while the first order is focused by a HPFS lens into the vacuum chamber.

## 3.2 Setup of the Intensity Stabilization

Fluctuations of intensity are a main issue in the design of optical dipole traps. They are responsible for a non constant trap potential which results in heating of the captured atoms [SOT97]. Also, for the matter of forced evaporative cooling, a stabilized, controllable trap potential is necessary to avoid fluctuations of  $v_{trap}$  (see figure 2.7). In the following, the setup of the intensity stabilization using a PID controller<sup>2</sup> is explained.

In the best case, the signal for the stabilization is received such that there is no influence on the intensity or the beam quality. This is achievable by using the transmission of a mirror, since they transmit about 1% of the incident beam.

Because the regulation is designed in a way that only the first order beam is stabilized, the transmitted zeroth order is blocked by an aperture. The transmission of the first order is splitted by a *polarizing beam splitter* (PBS). In this setup two different photodiodes are in use. This arrangement has the advantage of having a responsive diode in every intensity region. Therefore, the intensity stabilization is able to expand the lifetime of trapped atoms by a factor of 10 [FVD<sup>+</sup>07]. For laser powers of 200 W to 10 W, the less sensitive *silicon amplified photodetector* (PDA10A, Thorlabs) is active, while for  $< 10$  W a sensitive *biased InGaAs detector* (DET10N, Thorlabs) is the main source for the stabilization signal. In the high power range the silicon detector provides the noise signal, while the InGaAs detector adds a constant signal due to saturation. For low powers, the sensitive InGaAs detector contributes the noise signal, while the other

---

<sup>1</sup>The theory on acousto-optic modulators can be found in most literature on acousto-optics.

<sup>2</sup>A detailed view on PID controllers is given in [SLL09].

### 3.3 Transferring Atoms into the Optical Dipole Trap

detector adds a signal close to zero. Both signals are added and sent to an ADwin-Pro system (Jäger Messtechnik). The ADwin is used as PID controller which calculates the deviation from a priorly fixed setpoint and sends a counteracting signal to the RF-driver. The driver controls the power output for the AOM and, therefore, the proportion of power going into the first order.

By altering the setpoint, a required intensity in the first order can be adjusted and stabilized through the PID controller. This property is of advantage when performing an intensity ramp that carries out forced evaporative cooling. A detailed view on the cooling sequence will be given in section 3.3.

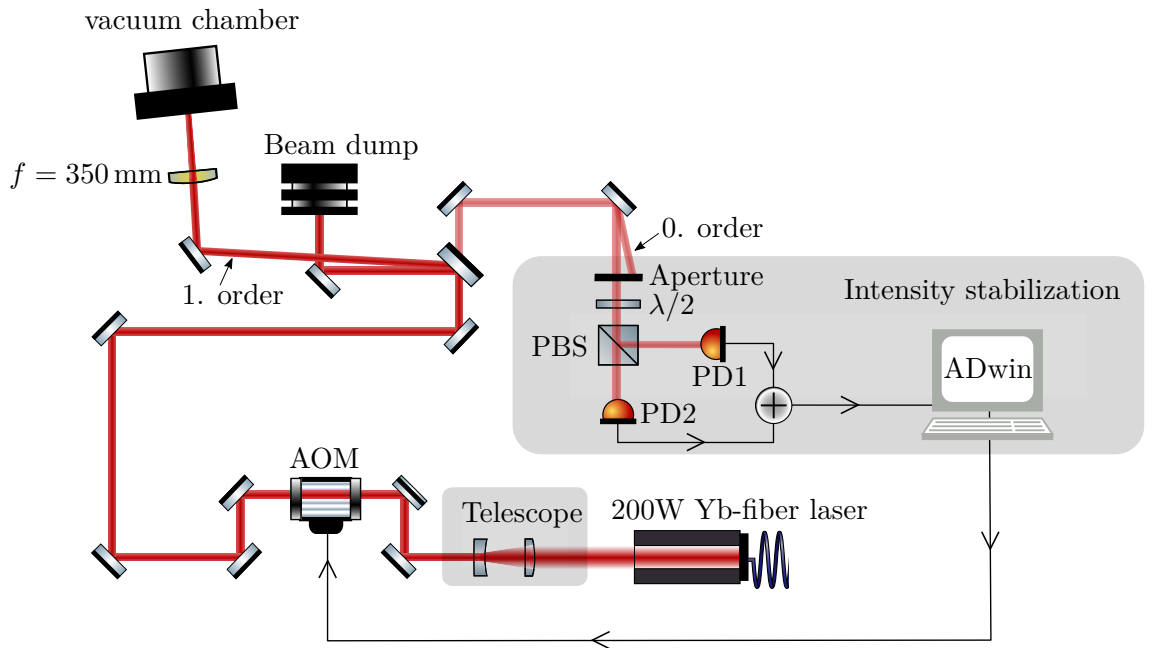


Figure 3.1: Experimental setup of the optical dipole trap

### 3.3 Transferring Atoms into the Optical Dipole Trap

This section provides an overview about how  ${}^6\text{Li}$  is trapped by the MOT and will be transferred into the optical dipole trap. In addition to that, the sequence of evaporative cooling is explained.

### 3 Implementation of an Optical Dipole Trap

A schematic overview of the whole experiment is given in figure 3.1. Within an oven with hot vapor of  ${}^6\text{Li}$  ( $\sim 300^\circ\text{C} - 500^\circ\text{C}$ ), atoms with an average velocity of  $\sim 1400 \frac{\text{m}}{\text{s}}$  are transferred via a thin tube into the main vacuum chamber. The three MOT beams are coming from fiber couplers which bridge the way from the MOT laser setup. Just behind the couplers, a PBS ensures the polarization of the beam. On the respective other side of the vacuum chamber, a mirror retro-reflects the incident beam. Thus, the beam passes twice through a  $\lambda/4$  waveplate which results in a total polarization change of  $\lambda/2$ . The MOT can only trap atoms within its capture range, which have a velocity below the capture velocity. Hence, the atoms are decelerated by a *Zeeman slower*. The slowing force in such an arrangement relies, just like in the MOT, on the Doppler shifted laser cooling technique with induced Zeeman shifts<sup>3</sup>. After loading the MOT with atoms for a few seconds, the atom number reaches an equilibrium.

In order to transfer atoms into the optical dipole trap, the dipole laser has to be arranged such that the focus overlaps with the center of the MOT. The transfer efficiency can be maximized by decreasing the size of the trapped gas cloud inside the MOT. From dimensions on the order of  $\sim 2\text{mm}$ , the lithium cloud needs to be compressed. This can be achieved by ramping the detuning close to resonance and decreasing the intensity, as minimum temperature and maximum confinement are given at  $\delta = -\gamma/2$  and  $s_0 = 2$  according to equation (2.9). The compression leads to a gain of transfer efficiency because the MOT cloud gets colder and denser. Therefore, the amount of atoms increases within the trapping volume of the focused dipole laser. With the use of setpoint modulation of the intensity stabilization (see previous section) the power is ramped down from the maximum output power of  $\sim 160\text{W}$  (at 80% AOM efficiency) to only a few mW. At the end of the sequence an ultracold quantum degenerate gas is left, given that rethermalization is efficient.

Until now the effect of high intensity laser beams was not discussed. Because of high powers, matter that the laser is traveling through heats up. The heating creates non neglectable changes of the initial alignment. For example, thermal effects in lenses shift the focal length and change properties of a focused beam. Since the optical dipole trap is constructed from a focused beam, a quantized analysis is carried out in the succeeding chapter.

---

<sup>3</sup> [PM82] explains the mechanism of a Zeeman slower in detail.

### 3.3 Transferring Atoms into the Optical Dipole Trap

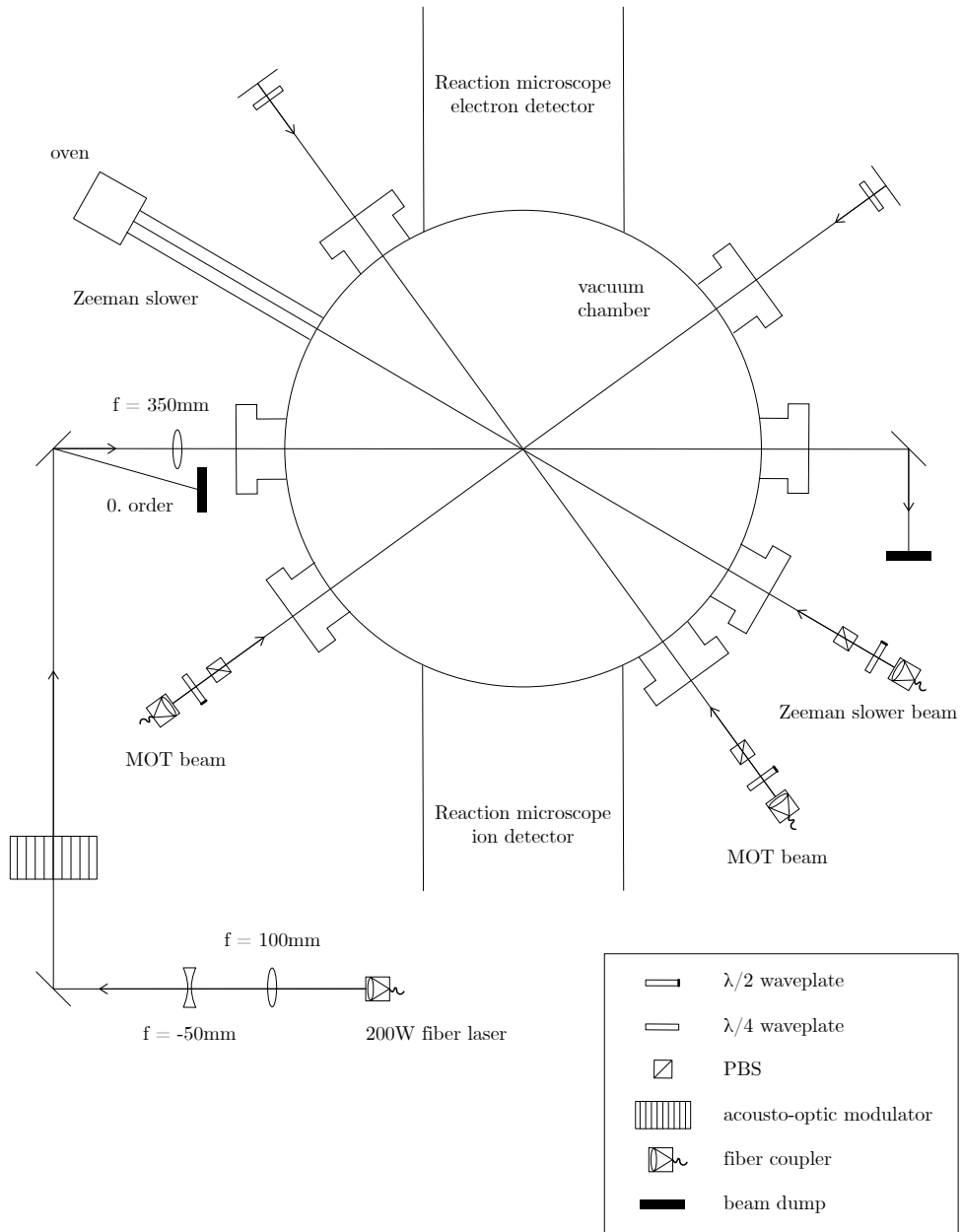


Figure 3.2: Schematic top-down view of the experimental setup at the MOTREMI. Therefore, only two of the three MOT beams are visible. Note that the optical dipole trap setup is simplified and only the first order passes through the chamber while the zeroth order is guided into the beam dump. For a detailed view see figure 3.1.

### *3 Implementation of an Optical Dipole Trap*

## 4 Consequences of High Intensity Lasers

In this chapter the consequences of high powers from the 200W Ytterbium fiber laser onto properties of the optical elements will be quantized. Before the measurements are presented, the basics on laser beams are described briefly.

### 4.1 Theory of Thermal Lensing

When laser powers reach regions of high intensity, interesting side effects occur. After the theory on Gaussian beams is introduced, the consequence of high intensities in optical elements is explained.

#### 4.1.1 The Gaussian Beam

Due to resonance conditions in the creation process, laser beams contain one or more modes. They are separable in longitudinal and transversal modes with respect to the propagation axis. For example, the used Ytterbium fiber laser is a longitudinal multi-mode laser with a spectral width of several nm, but in transversal direction it is nearly single-mode. The corresponding radiation field is classified in *transversal electromagnetic modes* (TEM). The TE-modes are distinguished by two indices which denote zeros of the electrical field in x- and y-direction, whereas z declares the propagation direction. Most laser beams are constructed that they only contain TEM<sub>00</sub> since it has the best optical properties for most applications in comparison to higher TE-modes. The intensity in these kind of beams is described by a Gaussian distribution (figure 4.1).

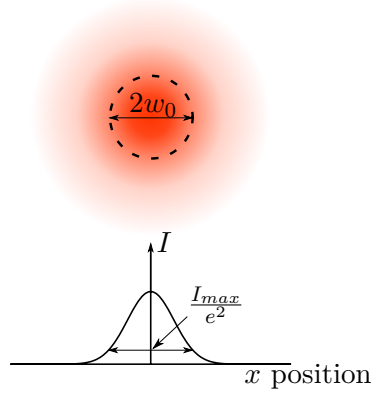


Figure 4.1: Top: Profile of a laser beam in TEM<sub>00</sub> seen from the axial propagation axis  
 Bottom: Corresponding intensity described by a Gaussian distribution in radial direction

While a Gaussian beam's intensity never actually drops off to zero, the beam radius  $w(z)$  is defined as the radial distance from the beam axis, at which the intensity dropped to the value  $I_{max}/e^2$ . In direction of propagation every Gaussian beam has a beam waist  $w_0$ , at which the beam radius has a minimum. The beam waist can either be virtual or real, that means it can be outside or within the source of radiation. The beam radius  $w(z)$  is symmetric around  $w_0$  and is given by [KL66]

$$w(z) = w_0 \sqrt{1 + \left( \frac{z - z_0}{z_R} \right)^2}, \quad (4.1)$$

where  $z_0$  denotes the axial position of  $w_0$ , and *Rayleigh range*  $z_R = \pi w_0^2 / \lambda$  ( $\lambda$  is the wavelength) at which the beam radius is  $w(z_R) = \sqrt{2}w_0$ .

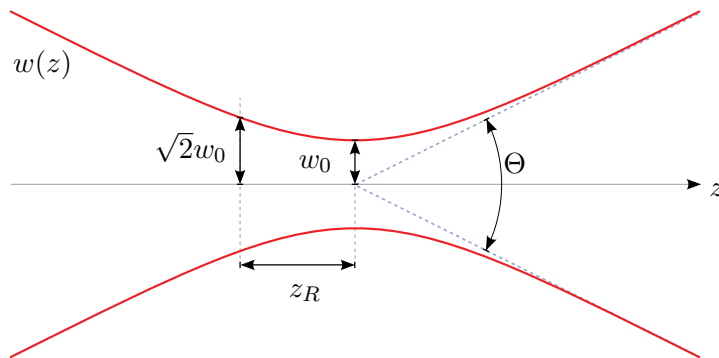


Figure 4.2: Transversal profile of a Gaussian beam

For  $z \gg z_0$  the beam radius  $w(z)$  increases linearly with  $z$  and can be approximated by

$$\Theta \simeq \frac{2\lambda}{\pi w_0}. \quad (4.2)$$

The beam parameter product for the fundamental Gaussian mode is defined as

$$\frac{w_0 \Theta}{2} = \frac{\lambda}{\pi}. \quad (4.3)$$

In the case that lasers do not contain TEM<sub>00</sub>, but higher modes or even mode mixtures, the beam waist  $w_0$  and the divergence angle  $\Theta$  increase with factor  $M$ . Therefore, equation (4.3) transforms to

$$\Theta_M \simeq M^2 \frac{2\lambda}{\pi w_0}, \quad (4.4)$$

where  $M^2$  is the so-called beam quality factor.

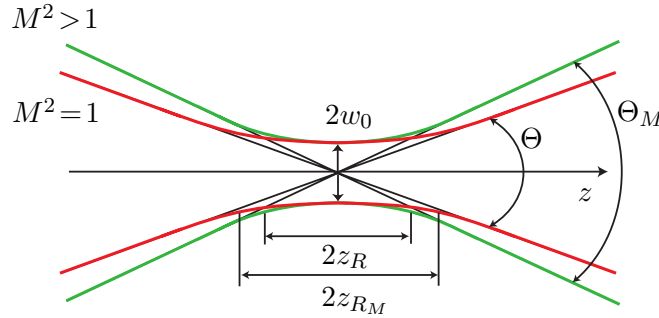


Figure 4.3: Growing beam waist of a Gaussian beam ( $M^2 = 1$ , red curve) compared to a beam of lower quality ( $M^2 > 1$ , green curve) with same beam waist  $w_0$ .

In case of high energy laser beams thermal effects lead to extraordinary behavior of optics and beam properties. A main source of deviation, the so-called thermal lensing, is presented in the following.

#### 4.1.2 The Thermal Lens

Working with high power laser beams results in non-neglectable side effects like thermal lensing. Due to absorption, it occurs in all materials that the laser passes through. Because the beam profile is Gaussian, a thermal gradient occurs in the element with a maximum at the highest beam intensity. Heating creates different density regions due to expansion of the material. Therefore, the refractive index differs from the initial one. Depending on

the material, an increasing temperature can lead to a lower or higher refractive index, indicated by a respectively negative or positive temperature coefficient. While this effect even occurs in air, most affected are the optical devices used in the setup. Particularly, lenses are sensitive to the thermal lensing effect since the laser propagates through the entire lens.

In order to simplify the effect consider a window with positive temperature coefficient inside of the beam path. As mentioned, a thermal gradient occurs inside of it, forming a convex lens with focal length  $f'$ . Consequently, the beam gets focused into that point. Adopting this concept to a lens instead of a window, it influences the initial focal length. In figure 4.4 the thermal gradient occurring in a convex lens is displayed. Due to a “thicker” lens the focal length decreases. For concave lenses the focus shift increases respectively.

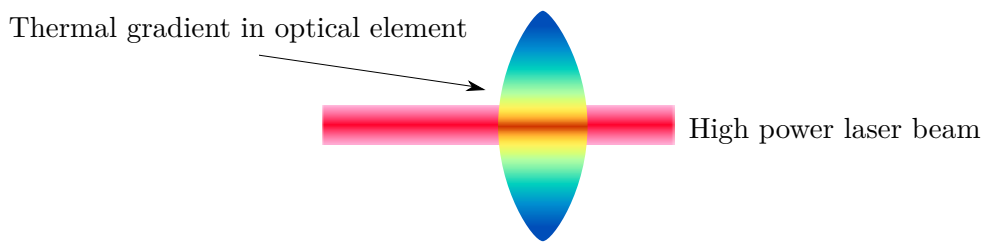


Figure 4.4: Schematic representation of thermal heating in a convex lens due to a high power laser beam. The colors of the thermal gradient denotes the temperature where red means high temperature and blue low temperature. Because of the temperature change, the material’s refractive index changes.

Lens materials used in this experiment have a positive temperature coefficient in the relevant temperature scale. Thus, the refractive index increases with growing temperature leading to a “thicker” lens [LF06].

## 4.2 Quantitative Observation of Thermal Effects

Hereinafter, the effect of high laser intensities on the beam quality and the experimental setup is investigated. The first section only determines the effect on  $M^2$  of the output beam. In the following section, the thermal effect on a custom made lens which focuses the beam into the vacuum chamber is compared to a regular N-BK7 lens. After that, the thermal lensing effect on the trap dimension within the vacuum chamber is observed.

### 4.2.1 Beam Quality

In addition to thermal lensing in the experimental setup, the initial beam properties can change because of thermal effects in the laser system and the optical fiber. For that reason, an investigation of  $M^2$  for different power outputs was carried out.

There is a standardized method of measurement by the ISO Standard 11146 [SSF<sup>+</sup>11] that requires ten measurements of the beam diameter. Five of them made within the Rayleigh length  $z_R$  and other five at a distance  $z > 2z_R$ . In order to obtain a more precise measurement, 18 data points were taken, with ten of them inside the Rayleigh length and four on each side at distance  $z > 2z_R$ . To obtain  $M^2$  from the data points, the following parabolic function is fitted:

$$d^2 = A + Bz + Cz^2 \quad (4.5)$$

with A, B, and C as fit parameter while d denotes the beam diameter. Equating the coefficients of (4.5), the beam parameters can be derived

$$z_0 = \frac{-B}{2C}, \quad d_0 = \sqrt{A - \frac{B^2}{4C}}, \quad \Theta = \sqrt{C}, \quad (4.6)$$

denoting the beam diameter  $d_0 = 2w_0$  at position  $z_0$  and divergence angle  $\Theta$  (see section 4.1.1). Using equation 4.4 the beam quality factor is

$$M^2 = \frac{d_0 \cdot \Theta \cdot \pi}{4\lambda}. \quad (4.7)$$

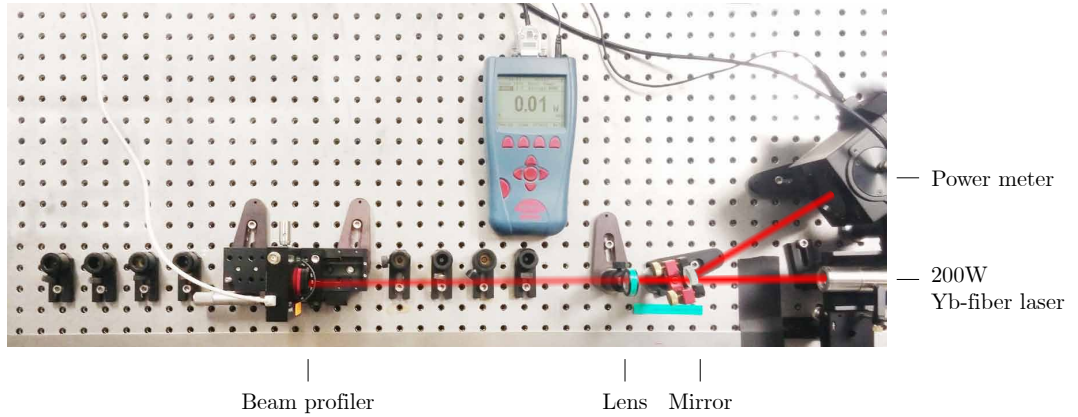


Figure 4.5:  $M^2$  measurement setup. The red line indicates the optical path of the laser. The blurred line demonstrates the transmitted proportion of the incident beam.

#### 4 Consequences of High Intensity Lasers

The measurement setup is shown in figure 4.5. In order to minimize systematic errors for the beam profiler position, the eight positions at which  $z > 2z_R$  are fixed by posts. For data points about the focal length of the lens, a linear micrometer shift was mounted, to obtain the beam profile position even more precisely. Data of the beam diameter in the x- and y-axis were taken for power outputs between 3 W and 210 W. The uncertainty of the beam diameter was given by the beam profiler which calculates the standard deviation through a set of roughly 100 images shot in a time frame of 5s. Due to astigmatism, thermal lensing, and uncertainties on the position of the beam profiler, the statistical errors on the data points had to be enlarged by a systematical error of 10%. By using equation (4.5) as fit function, one is able to calculate  $M^2$  with the help of equation (4.7). The fitting routine was carried out for all obtained data.

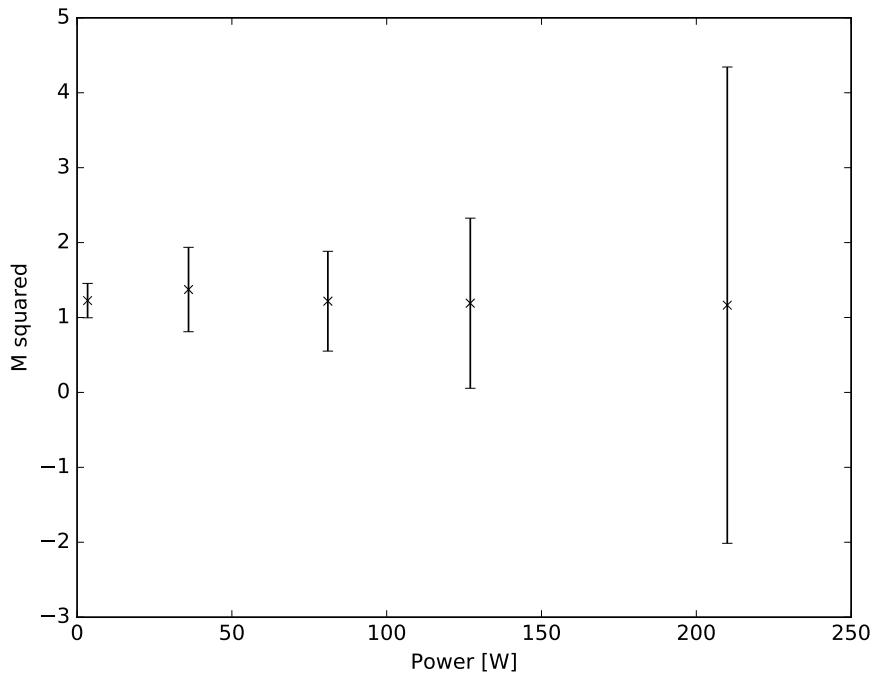


Figure 4.6: Beam quality factor  $M_x^2$  in dependence of laser power.

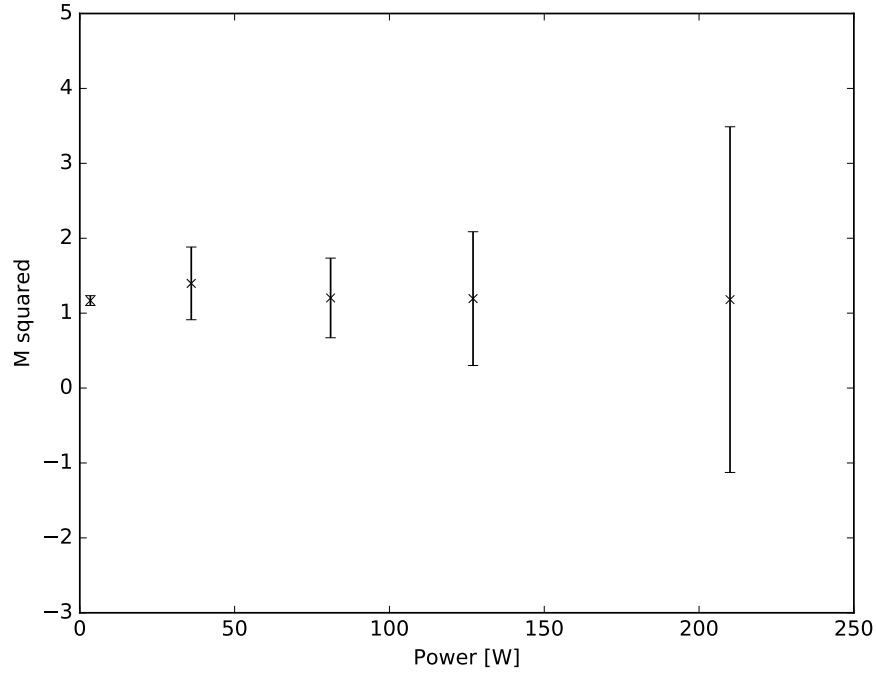


Figure 4.7: Beam quality factor  $M_y^2$  in dependence of laser power.

Figure 4.6 and 4.7 show the beam quality factor  $M_x^2$  and  $M_y^2$  for different power outputs. The fit for high intensities describes the data not as good as for the lower powers. Thus, relatively high uncertainties for higher powers are obtained. The calculated beam parameters from the fitting parameters provide realistic quantities for all powers, i.e.  $d_0 \approx 100 \mu\text{m}$  and  $\Theta \approx 15 \text{ mrad}$ . Thus, probably a thermal lens in the mirror, caused some additional side effects. With increasing power the thermal lens was responsible for growing irregularities during the measurement. However, the values for  $M_x^2$  and  $M_y^2$  do not show a remarkable divergence which is an indicator for a symmetrical shaped beam. Neglecting the increasing error bars, no distinct trend of a increasing or decreasing  $M^2$  is observable. For further calculations in section 4.2.3 the following values for 3 W are taken:

$$M_x^2 = (1.2 \pm 0.2)$$

$$M_y^2 = (1.17 \pm 0.07)$$

### 4.2.2 Focus Shift

In this section the effect of thermal lensing shifting the focus of a plano-convex lens for different power outputs of the Ytterbium fiber laser is investigated. Figure 4.8 shows the measurement setup. The used lenses are N-BK7 plano-convex lens with AR coating and a focal length of  $f = 400$  mm (LA1422-C, Thorlabs) and a *high purity fused silica* (HPFS) plano-convex lens with a focal length of  $f = 350$  mm (EscoOptics). The lenses have different material compositions. The HPFS lens contains lower proportions of OH-molecules which are responsible for absorption of infrared light. Hence, the HPFS lens should exhibit lower thermal effects.

Using equation (4.1) as fit function with fitting parameters  $w_0$  and  $z_0$ , one can measure position and beam radius of the focus. To determine the beam radius at certain axial points around the focus, a beam profiler was mounted to a linear motion stage. Since the laser power is too high and would damage the beam profiler, only the transmitted beam of a mirror is used. The reflected beam goes directly into a power meter head, which is capable of withstanding high laser intensities. This power meter head reads out the current output power.

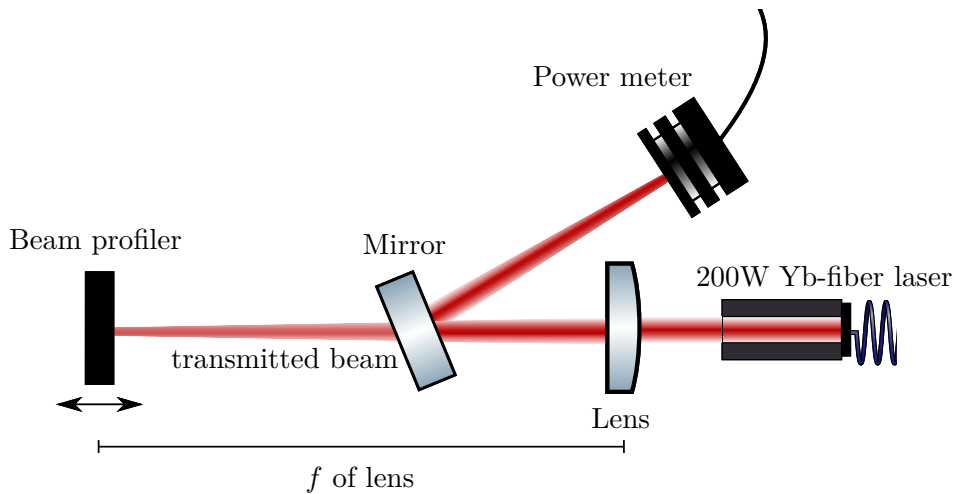


Figure 4.8: Experimental setup to obtain the focus shift. Due to high intensities a mirror guides the beam into a power meter. The transmitted beam is used for the measurement. In order to measure at different points the beam width, a beam profiler is moved on linear shift by a micrometer.

Different power levels between 8 W and 200 W were taken, while measuring the beam radius at 24 equidistant, axial points. The total position change of the beam profiler is  $\Delta x = 46$  mm. In theory the beam width expands as described in equation (4.1).

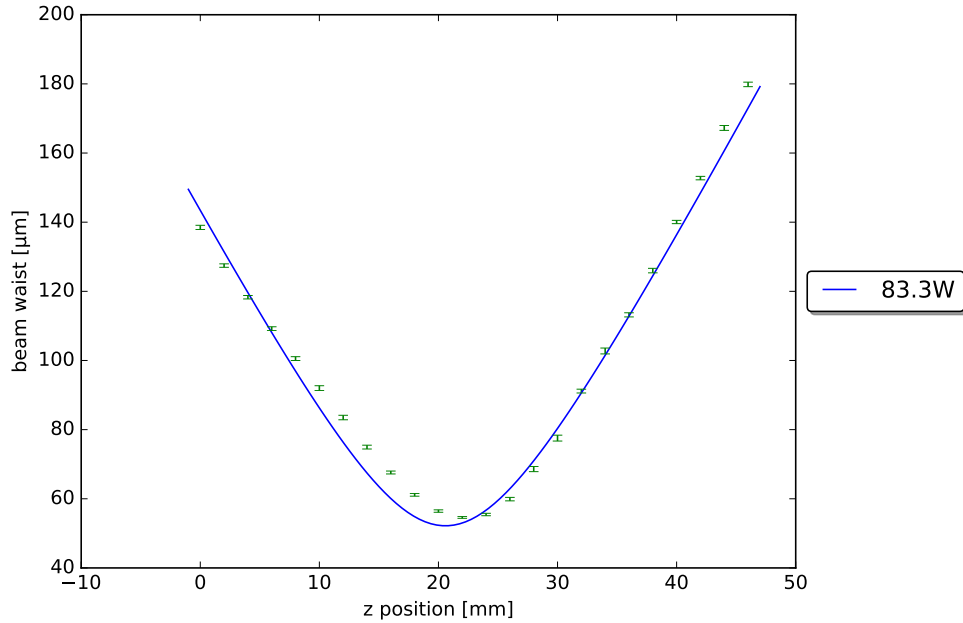


Figure 4.9: Plot of measured beam waist for different  $z$ -positions at an output power level of  $(83 \pm 2)\text{W}$ . The measurements are denoted by the green markers. The blue curve shows the fitted equation (4.1) to the data.

In figure 4.9 the beam radius in dependency of  $z$ -position is plotted for a power output of  $(83 \pm 2)\text{W}$ . The blue curve displays the fitted graph using equation (4.1) and the green marks show the measured data points. One recognizes an asymmetry of the data points, but according to equation (4.1) the beam waist should expand symmetrical in both directions seen from the focus point. This effect is not only occurring for a power output of  $(83 \pm 2)\text{W}$ , but in all measurements. The issue is probably due to irregularities or the creation of a thermal lens within the mirror. Fitting a symmetrical curve to the observed data points leads to wrong fit parameters. The attempt to solve the problem with two fit curves, one for the first half and the other for the second half of the data, did not lead to satisfactory results. Since all measurements show the same behavior, the focus coordinate  $z_0$  is estimated through fitting a smaller data set, which only contains five measuring points about the minimum measured beam radius. This analysis was repeated for different power levels and for both lenses. A plot of the power-dependent focus position is displayed in figure 4.10.

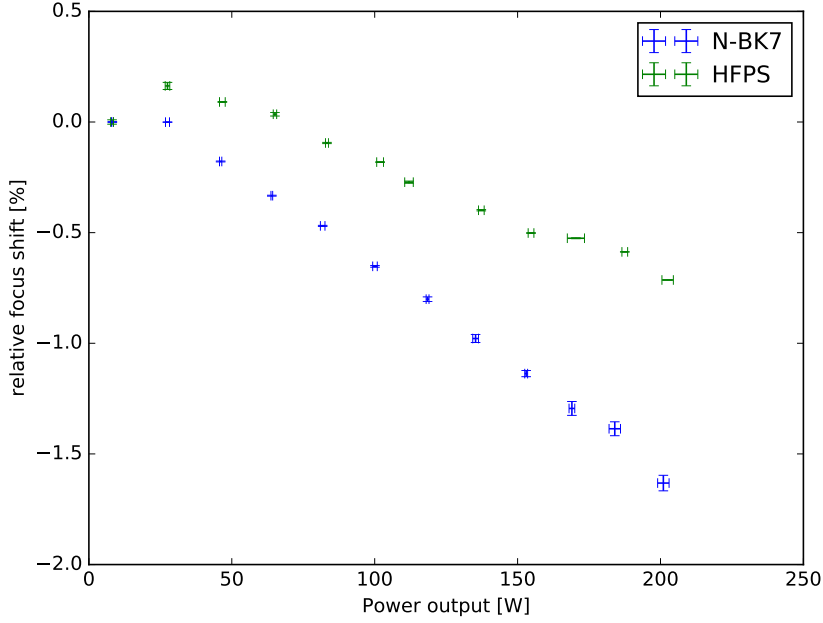


Figure 4.10: Relative focus shift plotted over power output for lenses made of N-BK7 (blue) and high fused pure silica (green). Negative shifts indicate a shorter focus distance from the lens.

Since both lenses have different focal length, the comparison is done by the relative focus change. Thus, the absolute focus position change is divided by corresponding focal length. A negative sign indicates a shorter focus point. Relative shifts from  $(8.2 \pm 0.3)$  W to  $(201.0 \pm 3.0)$  W are

$$\begin{aligned}\Delta f_{N-BK7} &= -(1.63 \pm 0.04) \% \\ \Delta f_{HFPS} &= -(0.71 \pm 0.01) \%\end{aligned}$$

while the total shifts are

$$\begin{aligned}\Delta f_{N-BK7}^{tot} &= -(6.53 \pm 0.14) \text{ mm} \\ \Delta f_{HFPS}^{tot} &= -(2.50 \pm 0.04) \text{ mm} .\end{aligned}$$

The plot shows a clear difference of thermal lensing for both lenses. As expected the HFPS lens shows a lower focus shift than the N-BK7 lens. Also, the collected data shows a decrease in the beam waist with growing

powers. From  $\omega_0 \approx 58 \mu\text{m}$  to  $\omega_0 \approx 51 \mu\text{m}$  for the HPFS lens and a change from  $\omega_0 \approx 67 \mu\text{m}$  to  $\omega_0 \approx 57 \mu\text{m}$  for the N-BK7 lens with respect to lowest and highest power output. This systematic deviation is probably attributed to thermal effects resulting in an effective shorter focal length. Thus, the effect of a decreasing focal length for both lenses fits well with the theory described in section 4.1.2.

### 4.2.3 Divergence Change

In section 4.2.2 only the thermal effect for one optical element was investigated. The actual experimental setup consists of many optical elements. Thus, a change of the focused beam properties in the vacuum chamber induced by heating of the whole setup is obtained in this section. Because a focus shift measurement cannot be done in the vacuum chamber, the influence on trap dimensions is observed.

According to (4.4), the beam waist  $w_0$  is inversely proportional to the divergence  $\Theta$ . Assuming the output beam has constant  $M^2$ , the determination of  $\Theta$  is sufficient to find relative changes of the beam waist.

To measure the beam divergence only a very simple architecture is needed. A schematic overview is given in figure 4.12. One lens and the beam profiler is used for the measurement, while a mirror guides the high intensity laser into the beam dump. Like in previous measurements only the transmitted beam is used for the measurement. In order to obtain the divergence of a beam the profiler is placed into the exact focal length of the lens (see figure 4.11). In such an arrangement the divergence of a beam is [DS78]

$$\Theta = \frac{d}{f} \quad (4.8)$$

where  $d$  denotes the beam diameter at focal length  $f$ .

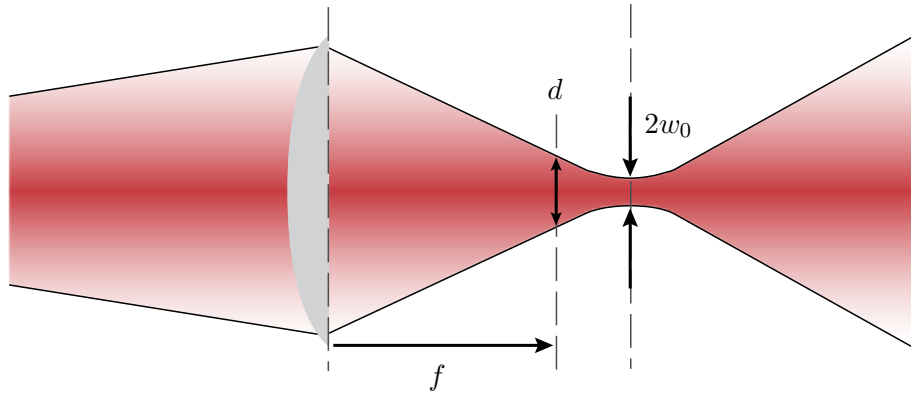


Figure 4.11: Principle of divergence measurement for non collimated beams

#### 4 Consequences of High Intensity Lasers

A big advantage of this rather small measurement setup is that it can be built up easily on the other side of the vacuum chamber. The measured beam is the frequency shifted first order from the AOM. After the alignment procedure the power in the first order was about 50% of the incident beam.

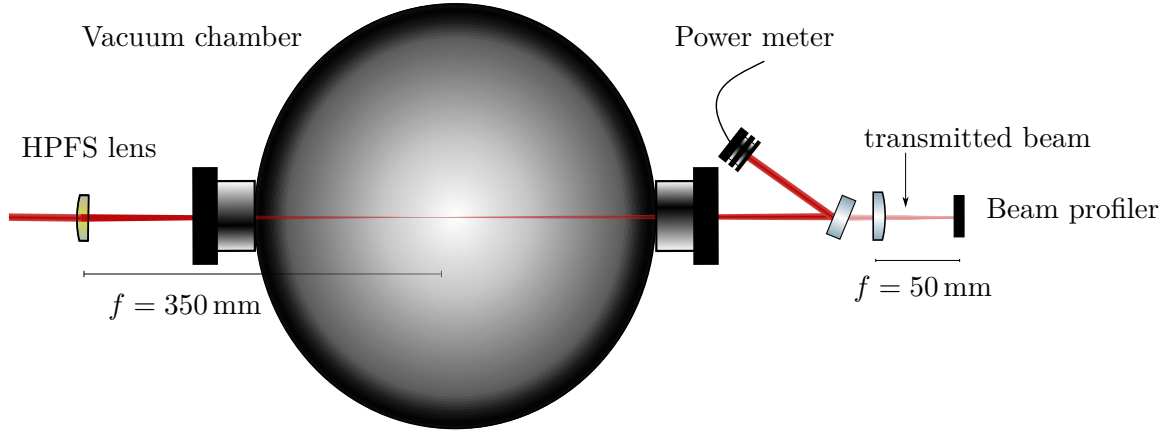


Figure 4.12: Setup to measure divergence changes of the beam after passing through the experimental setup and being focused by a HPFS lens ( $f = 350$  mm). Afterwards the beam is guided by a mirror into the power meter and only the transmitted beam is taken for measurements.

Not only divergence differences for two power levels  $\sim 2$  W and  $\sim 100$  W were measured, also the time-dependent change of  $\Theta(t_{exp})$  for both powers. In this context the time-dependency means how long the laser is exposed onto the optical parts. Therefore, the measurement provides information about the heating rate in the experimental setup.

For exposure times between 1 ms and 5 s the beam diameter in x-direction  $d_x$  as well as in y-direction  $d_y$  was obtained with the beam profiler. In order to obtain higher accuracy, three measurement points for each time were taken. The divergence, therefore, is given by using (4.8) while the uncertainty is given by  $\Delta f = \pm 1$  mm and standard deviation of  $\bar{d}_x$  and  $\bar{d}_y$  respectively.

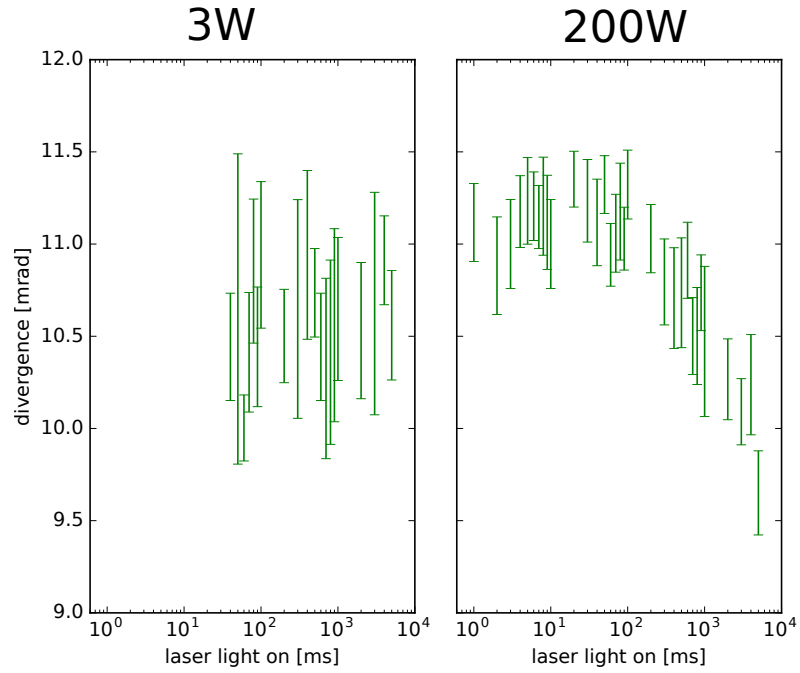


Figure 4.13: Divergence measurements in x-direction  $\Theta_x$  in dependence of exposure time  $t_{exp}$  for a power output of 3 W and 200 W.

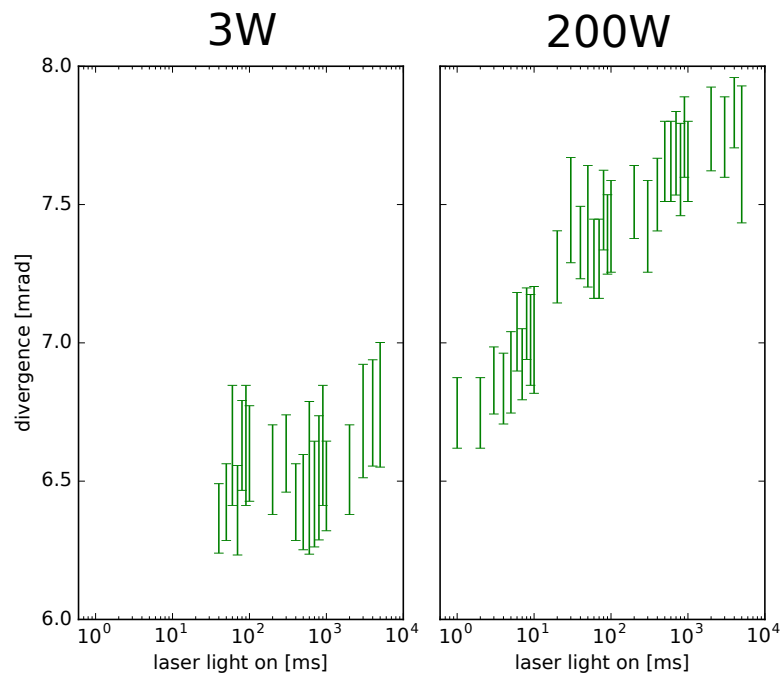


Figure 4.14: Divergence measurements for y-direction  $\Theta_y$  in dependence of exposure time  $t_{exp}$  for a power output of 3 W and 200 W.

The beam was of an elliptic shape, thus, data was taken for  $\Theta_x$  and  $\Theta_y$ . Also, the exposure time of the beam profiler for low intensities had to be at least 40 ms in order to obtain a sufficient beam profile.

It can be seen from figures 4.13 and 4.14 that for exposure times of a few ms the divergence value is approximately the same as for relatively low power. Therefore, the influence of heating due to the high intensity is neglectable at low exposure times. In the following, the divergence value at  $t_{exp} = 1\text{ms}$  will be used as reference point to quantify thermal effects. Both figures show a notable divergence change for increasing exposure times. It is worth mentioning that  $\Theta_x$  and  $\Theta_y$  have opposite directions of change for rising exposure times. This means that the beam becomes more circular for higher intensities.

Using the obtained values for  $M_x^2 = (1.2 \pm 0.2)$  and  $M_y^2 = (1.17 \pm 0.07)$  (where the indexes denote x- and y-axis respectively) from section 4.2.1, one can calculate the trap dimension changes with respect to longer exposure times for 200 W. Note, that the used values are obtained for the power output of 3 W, because the obtained values for the high power region have too large uncertainties. However, for 200 W and low  $t_{exp}$ , this seems to be a reasonable approach, since the divergences are nearly the same as for the low power output. The only additional assumption made, is that  $M_x^2$  and  $M_y^2$  are constant for all  $t_{exp}$ . Using the divergence values at  $t_{exp} = 1\text{ms}$  as initial trap size and for comparison the divergence at  $t_{exp} = 5\text{s}$ , the discrepancy can be determined. The following table shows the beam waist according to (4.2).

Axis	$w_0@1\text{ms}$ [ $\mu\text{m}$ ]	$w_0@5\text{s}$ [ $\mu\text{m}$ ]	$\Delta w_0$ [ $\mu\text{m}$ ]	$\Delta w_0$ [%]
X	73(12)	84(14)	11(18)	15(25)
Y	117(8)	103(8)	14(11)	12(9)

Table 4.1: Beam waist for x-axis at different exposure times and the effective change due to heating

Axis	$z_R@1\text{ms}$ [mm]	$z_R@5\text{s}$ [mm]	$\Delta z_R$ [mm]	$\Delta z_R$ [%]
X	16(5)	21(7)	5(9)	31(57)
Y	40(6)	31(5)	11(8)	28(21)

Table 4.2: Corresponding Rayleigh length  $z_R = \pi w_0^2/\lambda$

From tables 4.1 and 4.2 one can calculate the effective trap volume by

## 4.2 Quantitative Observation of Thermal Effects

approximation that the trap has ellipsoidal shape. The axial dimension is determined by the mean of  $z_R^x$  and  $z_R^y$  (the superscript denotes the x- and y-axis respectively) while the radial dimension is  $w_0^x$  and  $w_0^y$ . Thus, the trap volumes are

$$\begin{aligned} @ 1 \text{ ms:} & \quad V_{trap} = (1.00 \pm 0.15) \text{ mm}^3 \\ @ 5 \text{ s:} & \quad V_{trap} = (0.94 \pm 0.17) \text{ mm}^3 . \end{aligned}$$

Mostly the standard deviation from  $M_x^2$  and  $M_y^2$  cause the relatively high uncertainties of the trap volumes. The first change of the divergence can be seen for an exposure time of  $t_{exp} \approx 5 \text{ ms}$  for  $\Theta_y$  and at exposure time  $t_{exp} \approx 100 \text{ ms}$  for  $\Theta_x$ .



## 5 Conclusion and Outlook

Within this thesis a major part, an optical dipole trap, was set up for the MOTREMI experiment. The trap is designed as a single focused-beam trap with the possibility of an extension to a cross-over setup. The new trap is a starting point for further cooling of  ${}^6\text{Li}$  from a MOT to temperatures on the order of a hundred nK. Fluctuations in the initial output power would lead to significant losses during the cooling process [SOT97]. For that purpose, an intensity stabilization has been constructed. The feedback loop comprises an AOM and two different photodiodes, which ensure a stabilization for all output powers. Since the further proceeding requires evaporative cooling, the intensity stabilization provides the perfect starting point. By ramping the intensity relatively smooth through simultaneous tuning and stabilization, the trap will be able to cool very efficient. The high power, far red-detuned light is provided by a 200W Ytterbium fiber laser. The output beam has an almost perfect Gaussian intensity distribution operating at  $\lambda = 1070\text{ nm}$ . Due to inefficiencies of the AOM, a maximum power of  $\sim 160\text{ W}$  is available to form the trap.

Furthermore, property changes of optical elements caused by high laser power have been investigated. In the first step, the beam quality factor  $M^2$  in x- and y-direction was measured for different power outputs. Because of the relatively high uncertainties with growing intensity, no quantitative statement on the trend of  $M^2$  can be given. However, the obtained values indicate a constant  $M^2$  in both directions. Additionally, the data implicates a symmetric beam profile.

From the next measurement, the decreasing focal length for lenses made from N-BK7 and high purity fused silica was observed. The beam diameter around the focus was obtained for 26 measurement points. The predicted focus shift was seen in both lenses, while the thermal lensing effect led to a shorter focal length. It has been found that the N-BK7 lenses diverge stronger in comparison to HPFS lenses:

$$\begin{aligned}\Delta f_{N-BK7} &= -(1.63 \pm 0.04) \% , \\ \Delta f_{HPFS} &= -(0.71 \pm 0.01) \% ,\end{aligned}$$

where the values indicate the percentage deviation from the original focus position, while a negative sign indicates shorter focal length.

From the divergence measurement for a power output of 200 W, the trap

## 5 Conclusion and Outlook

volumes at different exposure times have been calculated to

$$\begin{aligned} @ 1 \text{ ms:} & \quad V_{trap} = (1.00 \pm 0.15) \text{ mm}^3 \\ @ 5 \text{ s:} & \quad V_{trap} = (0.94 \pm 0.17) \text{ mm}^3 . \end{aligned}$$

Due to the uncertainties in the obtained volumes, it cannot be stated that the trap size changes. Nonetheless, the data shows an effective change of the beam profile to a more circular one for growing exposure times, due to opposite directions of  $\Theta_x$  and  $\Theta_y$ . Even though, a change in the trap volume could not be estimated precisely, the time it takes until thermal effects set in, is of greater interest:

$$\begin{aligned} \Theta_y : & \quad t_{exp} \approx 5 \text{ ms} , \\ \Theta_x : & \quad t_{exp} \approx 100 \text{ ms} . \end{aligned}$$

These observations can be seen as threshold values and will help in the latter realization of the evaporative cooling sequence. Adjusting the exposure time for high powers in the setup can counteract unpredictable shifts in the initial alignment.

# Bibliography

- [AEM<sup>+</sup>95] M. H. Anderson, J. R. Ensher, M. R. Matthews, C. E. Wieman, and E. A. Cornell. Observation of bose-einstein condensation in a dilute atomic vapor. *Science*, 269(5221):198, Jul 14 1995. Copyright - Copyright American Association for the Advancement of Science Jul 14, 1995; Last updated - 2010-06-08; CODEN - SCIEAS.
- [DS78] GW Day and CF Stubenrauch. Laser far-field beam-profile measurements by the focal plane technique. *NASA STI/Recon Technical Report N*, 78, 1978.
- [FVD<sup>+</sup>07] Jurgen Fuchs, Gopi Veeravalli, Paul Dyke, Eva Kuhnle, Grainne Duffy, Chris J. Vale, Peter Hannaford, and Wayne Rowlands. Molecular bec in a low power crossed dipole trap. In *Quantum-Atom Optics Downunder*, page QThB2. Optical Society of America, 2007.
- [GRJ03] Markus Greiner, Cindy A Regal, and Deborah S Jin. Emergence of a molecular bose-einstein condensate from a fermi gas. *Nature*, 426(6966):537–540, 2003.
- [GWO00] Rudolf Grimm, Matthias Weidemüller, and Yurii B Ovchinnikov. Optical dipole traps for neutral atoms. *Advances in atomic, molecular, and optical physics*, 42:95–170, 2000.
- [KL66] H. Kogelnik and T. Li. Laser beams and resonators. *Appl. Opt.*, 5(10):1550–1567, Oct 1966.
- [Let07] Vladilen S. Letochov. *Laser control of atoms and molecules*. Oxford University Press, Oxford [u.a.], 1. publ. edition, 2007.
- [LF06] Douglas B Leviton and Bradley J Frey. Temperature-dependent absolute refractive index measurements of synthetic fused silica. In *SPIE Astronomical Telescopes+ Instrumentation*, pages 62732K–62732K. International Society for Optics and Photonics, 2006.
- [Mes07] Dieter Meschede. *Optics, Light and Lasers*. Physics textbook. Wiley-VCH, Weinheim, 2., rev. and enlarg. ed. edition, 2007.

## Bibliography

- [MS99] Harold J. Metcalf and Peter van Straten. *Laser cooling and trapping*. Graduate texts in contemporary physics. Springer, New York ; Berlin ; Heidelberg [u.a.], 1999.
- [PM82] William D. Phillips and Harold Metcalf. Laser deceleration of an atomic beam. *Phys. Rev. Lett.*, 48:596–599, Mar 1982.
- [SLL09] Su Whan Sung, Jietae Lee, and In-Beum Lee. *Process identification and PID control*. Wiley, Singapore, 2009.
- [SOT97] T. A. Savard, K. M. O’Hara, and J. E. Thomas. Laser-noise-induced heating in far-off resonance optical traps. *Phys. Rev. A*, 56:R1095–R1098, Aug 1997.
- [SSF<sup>+</sup>11] Oliver A Schmidt, Christian Schulze, Daniel Flamm, Robert Brüning, Thomas Kaiser, Siegmund Schröter, and Michael Duparré. Real-time determination of laser beam quality by modal decomposition. *Optics express*, 19(7):6741–6748, 2011.
- [Ste07] Jochen Steinmann. *Multiphoton ionization of laser cooled lithium*. 2007.

# Erklärung

Ich versichere, dass ich diese Arbeit selbstständig verfasst und keine anderen als die angegebenen Quellen und Hilfsmittel benutzt habe.

Heidelberg, den 18.04.2017

Lars Heinen